Chemistry–A European Journal

Research Article
doi.org/10.1002/chem.202200100

Chemistry Europe
European Chemical
Societies Publishing

www.chemeurj.org

A New Class of Task-Specific Imidazolium Salts and Ionic Liquids and Their Corresponding Transition-Metal Complexes for Immobilization on Electrochemically Active Surfaces

Vera Seidl,[a] Angel H. Romero,[a, e] Frank W. Heinemann,[a] Andreas Scheurer,[a] Carola S. Vogel,[b] Tobias Unruh,[b] Peter Wasserscheid,[c, d] and Karsten Meyer*[a]

Dedicated to Professor Holger Braunschweig on the occasion of his 60th birthday

Abstract: Adding to the versatile class of ionic liquids, we report the detailed structure and property analysis of a new class of asymmetrically substituted imidazolium salts, offering interesting thermal characteristics, such as liquid crystalline behavior, polymorphism or glass transitions. A scalable general synthetic procedure for *N*-polyaryl-*N'*-alkyl-functionalized imidazolium salts with *para*-substituted linker (L) moieties at the aryl chain, namely $[LPh_mIm^HR]^+$ (L = Br, CN, SMe, CO_2Et, OH; $m = 2, 3$; R = C_{12}, PEG_n; $n = 2, 3, 4$), was developed. These imidazolium salts were studied by single-crystal X-ray diffraction (SC-XRD), NMR spectroscopy and thermochemical methods (DSC, TGA). Furthermore, these imidazolium salts were used as N-heterocyclic carbene (NHC) ligand precursors for mononuclear, first-row transition metal complexes (Mn^{II}, Fe^{II}, Co^{II}, Ni^{II}, Zn^{II}, Cu^I, Ag^I, Au^I) and for the dinuclear Ti-supported Fe-NHC complex $[(OPy)_2Ti(OPh_2ImC_{12})_2(FeI_2)]$ (OPy = pyridin-2-ylmethanolate). The complexes were studied concerning their structural and magnetic behavior via multi-nuclear NMR spectroscopy, SC-XRD analyses, variable temperature and field-dependent (VT-VF) SQUID magnetization methods, X-band EPR spectroscopy and, where appropriate, zero-field ^{57}Fe Mössbauer spectroscopy.

[a] V. Seidl, Dr. A. H. Romero, Dr. F. W. Heinemann, Dr. A. Scheurer, Prof. Dr. K. Meyer
Friedrich-Alexander-Universität Erlangen-Nürnberg (FAU), Department Chemie und Pharmazie, Anorganische Chemie
Egerlandstraße 1, 91058 Erlangen (Germany)
E-mail: karsten.meyer@fau.de

[b] Dr. C. S. Vogel, Prof. Dr. T. Unruh
Friedrich-Alexander-Universität Erlangen-Nürnberg (FAU), Department Physik, Institut für Physik der kondensierten Materie
Staudtstraße 3, 91058 Erlangen (Germany)

[c] Prof. Dr. P. Wasserscheid
Friedrich-Alexander-Universität Erlangen-Nürnberg (FAU), Department Chemie- und Bioingenieurwesen
Egerlandstraße 3, 91058 Erlangen (Germany)

[d] Prof. Dr. P. Wasserscheid
Forschungszentrum Jülich
Helmholtz-Institute Erlangen-Nürnberg for Renewable Energy (IEK11)
Egerlandstraße 3, 91058 Erlangen

[e] Dr. A. H. Romero
Grupo de Química Orgánica Medicinal, Instituto de Química Biológica
Facultad de Ciencias, Universidad de la República
Montevideo 11400 (Uruguay)

Introduction

Ionic liquids (ILs), generally defined as salts with a melting point below 100 °C,[1] have attracted growing interest since the beginning of the 21st century.[2] Due to the variety of bulky, low symmetric organic cations and (in)organic anions,[3] ionic liquids offer swiftly tunable physical and chemical properties. This results in a unique property profile, such as negligible vapor pressure, non-flammability, excellent tribological behavior, high conductivity, and an extraordinary (electro-)chemical stability (e.g. wide electrochemical window). The properties, originating from their liquid state at moderate or even ambient temperatures, make ILs attractive for a variety of applications.[4]

Offering almost limitless possibilities of functionalization, ILs – most commonly imidazolium-based ILs – can be designed with tailor-made properties and reactivity. These so-called task-specific ionic liquids (TSILs) are mainly used for particular applications in catalysis, organic synthesis, material separation as well as for the synthesis of nanostructured or ion conductive materials.[5] For example, the incorporation of a carboxylic acid dissolves metals and metal oxides,[6] whereas imidazolium salts bearing an amine functionality can separate CO_2 from gas streams.[7]

Introducing an aryl chain at the imidazolium core simultaneously provides ample space for substitution chemistry and the opportunity for tuneability of electronic communication. This influences the molecules' electronic and physicochemical properties remarkably. For instance, non-covalent π-π interac-

Chem. Eur. J. **2022**, *28*, e202200100 (1 of 13)

© 2022 The Authors. Chemistry - A European Journal published by Wiley-VCH GmbH

Chemistry–A European Journal

Research Article
doi.org/10.1002/chem.202200100

Chemistry Europe
European Chemical
Societies Publishing

tions, important for specific industrial applications, such as extraction separation, catalytic reactions, and self-assembled materials, are possible due to the extended aromatic system of the rigid-core aryl-substituted ILs.[8]

Towards more hydrophilic side chains for imidazolium salts, methylated poly(ethylene glycol) (mPEG) is a prominent example.[9] Possessing polarity and lacking reactive functional groups, PEGylation of an IL changes its physicochemical behavior without significantly changing the reactivity. Hence, a decrease of the melting point but an increase of the thermal stability is induced.[10] Owing to moderate electric conductivity (in the order of 0.1 mS cm^{-1}) combined with a low viscosity, PEG-substituted ILs can be excellently applied as electrolytes in electronic devices.[11] Moreover, the possibility of interacting with (in)organic cations and small molecules enables PEG chains to coordinate and conduct protons; and thus, they find application in gas separation membranes[12] and in the synthesis and stabilization of nanoparticles.[13]

Based on our experience with saturated and unsaturated, imidazolium-based ILs,[3a,14] we herein report new synthetic strategies as well as characterization and reactivity studies of asymmetrically substituted ILs. Combining advantages of aryl and PEG-substitution, we developed *N*-polyaryl and *N'*-PEG$_n$ (*n* = 2, 3, 4) substituted imidazolium salts (with PEG$_n$ = (–CH$_2$–CH$_2$–O)$_n$–CH$_3$). For interaction or adsorption of these salts on a solid support, the attachment of an appropriate linker functionality (L) at the phenyl moiety was required (Figure 1).

This protocol leads to an IL with the general abbreviation [LPh$_m$Im^{H}R][A] (Ph = 1,4-phenylene, *m* = 2, 3; R = PEG$_n$, C$_{12}$H$_{25}$; *n* = 2, 3; A = anion). Due to their composition, these types of imidazolium salts can provide the opportunity to link a surface

and a catalytically active site via electron transfer along the aryl chain.

Aryl-alkyl substituted ILs, similar to the imidazolium salts presented herein, are also reported in literature, for example as tunable aryl alkyl ionic liquids (TAAILs);[8a,15] notably, some biphenyl-functionalized imidazolium salts are also known for ionic liquid crystalline behavior, when substituted with long alkyl chains at the aryl and/or imidazole moiety.[16] So-called ionic liquid crystals (ILCs) – combining ionic liquids (see above) and liquid crystals properties (dynamic molecular order, anisotropic physical properties, etc.) – are coveted materials for organized or ion-conductive processes.[17]

Providing reactivity for potential (electro)chemical catalysis, transition metal complexes with N-heterocyclic carbene (NHC) ligands are promising and well-known examples.[18] The complexes described herein include mainly first-row divalent transition metals (Mn^{II}, Fe^{II}, Co^{II}, Ni^{II}, Zn^{II}) as well as the monovalent group 11 metals (Cu^I, Ag^I, Au^I), based on the [BrPh$_2$Im^{H}PEG$_n$]I and [NCPh$_2$Im^{H}PEG$_3$]I ILs as carbene precursors.

In order to model the surface behavior of an immobilized IL (e.g. on TiO$_2$), we implemented a homogenous model system for structural and chemical studies. For that purpose, we developed imidazolium salts with a linker group supported by titanium in a 2:1 fashion (IL:Ti); i.e., one Ti(IV) center is coordinated by the linker of two imidazolium salts. Using the [HOPh$_2$Im^{H}C$_{12}$]$^+$ salt, the phenolate functionality is coordinated to a titanium precursor resulting in a [(OPy)$_2$Ti(OPh$_2$Im^{H}C$_{12}$)$_2$]$^{2+}$ complex (**21**) (OPy = pyridin-2-ylmethanolate). In contrast to surface adsorbed ILs, these complexes can be easily characterized regarding their structural and electronical properties. Moreover, an additional transition metal (e.g. iron) can be introduced via transformation of the imidazolium salt to a NHC ligand (**22**).

Results and Discussion

N-Polyaryl *N'*-alkyl substituted imidazolium salts

Synthesis

The synthetic route to all imidazolium salts described herein is based on C–C/C–N cross-coupling strategies and alkylation reactions (Scheme 1). In order to simplify the reaction scheme, all protecting and deprotecting steps are omitted for clarity (for details, see Supporting Information).

The *N*-(bromophenyl)imidazole and *N*-(bromo[1,1']biphenyl)imidazole starting materials were synthesized according to slightly modified literature protocols, using a Radziszewski ring closure[15a,19] and an Ullmann cross-coupling reaction,[20] respectively. The desired linker functionality and the elongated aryl chain are introduced by Suzuki-Miyaura cross-coupling reactions of the corresponding *para*-functionalized phenyl boronic acids.[21] Therefore, [Pd(dppf)Cl$_2$]·CH$_2$Cl$_2$ (dppf = 1,1'-bis(diphenylphosphino)ferrocene) or [Pd(PPh$_3$)$_4$] (PPh$_3$ = triphenylphosphine) were used as catalysts in THF/H$_2$O mixtures and potassium carbonate as a base. Alkylation of the *N*-

m	*n*	L	A			L	A	
2	2	Br	I	**1**		Br	I	**10**
2	3	Br	I	**2-I**		OH	I	**11-I**
2	3	Br	BF$_4$	**2-BF$_4$**		OH	PF$_6$	**11-PF$_6$**
2	3	Br	PF$_6$	**2-PF$_6$**				
2	3	CN	I	**3**				
2	3	COOEt	I	**4**				
2	3	OH	I	**5**				
2	3	SMe	I	**6**				
2	4	Br	I	**7**				
3	3	COOEt	I	**8**				
3	3	SMe	I	**9**				
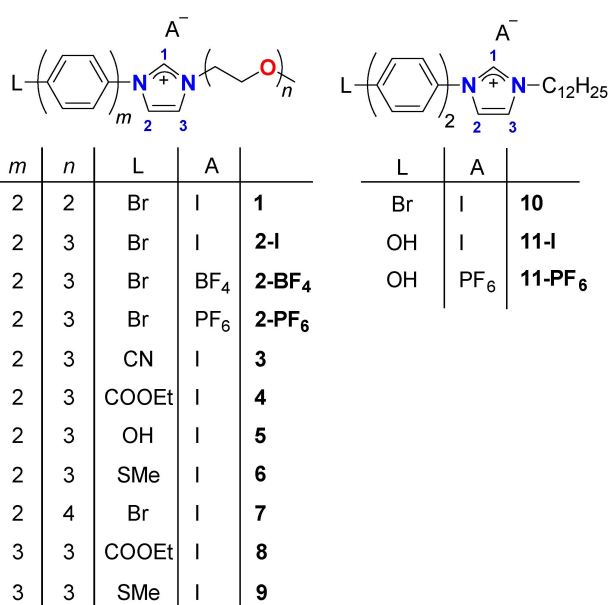
Figure 1. Overview of the synthesized ILs **1–11**. The numbering (dark blue) of the imidazolinium moiety correlates with the atom labeling in the X-ray diffraction analyses, and is used for further discussion.
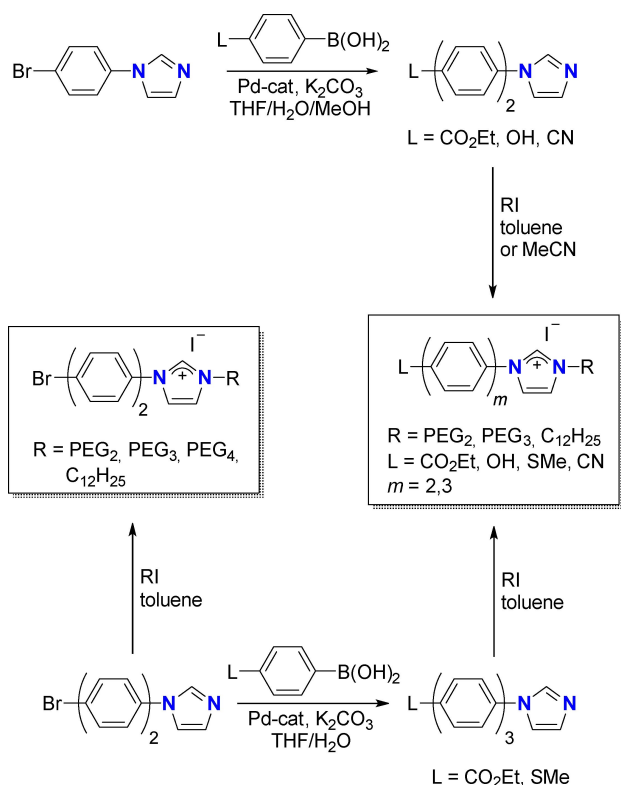
Scheme 1. Synthetic routes to all prepared imidazolium salts $[LPh_mIm^HR]I$.

(polyphenyl)imidazole with the respective alkyl or PEG_n iodide, in toluene or acetonitrile, yields the desired ILs **3–6**, **8**, **9**, and **11**. Note, the use of alkyl chlorides or bromides leads to unsatisfying reaction yields. All bromide substituted imidazolium salts (**1**, **2-I**, **7**, **10**) were synthesized via direct alkylation of N-(bromo[1,1']biphenyl)imidazole. Anion exchange of the iodide salts was carried out in organic media with the corresponding silver or potassium salts resulting in compounds **2-BF$_4$**, **2-PF$_6$**, and **11-PF$_6$**. Because of their convenient synthetic procedure, imidazolium salts with bromide (**2**) and carboxylic ester linker units (**4**) are mainly used for structural studies (see below). For immobilization on electrochemically active surfaces, those linkers are easily exchangeable by other entities, for example thioethers or cyanides for gold surfaces.[22]

All imidazolium salts were dried under vacuum for 2 days and characterized by *CHN* elemental combustion analysis, NMR spectroscopy as well as differential scanning calorimetry (DSC) and thermogravimetric analysis (TGA). In addition, compounds **1**, **2-I**, **2-PF$_6$**, and **4** were studied by single-crystal X-ray diffraction (SC-XRD) analysis.

According to ^1H NMR spectroscopy, the signal of the imidazolium C(1)—H proton is high-field shifted depending on the anion by the order of $I^- > [PF_6]^- > [BF_4]^-$. Such anion dependency is also known in literature[23] and indicates an increasing hydrogen bonding strength and therefore, stronger ion pairing in solution.

Solid-state molecular structures

Single-crystals of $[BrPh_2Im^HPEG_n][A]$ ($n = 2$, 3; $A = I^-$, PF_6^-) (**1**, **2**), suitable for SC-XRD, were obtained by slow diffusion of chloroform/diethyl ether (for **1**), methanol/dichloromethane (for **2-PF$_6$**) or from a cold saturated methanolic solution (for **2-I**). Single-crystals of $[EtO_2CPh_2Im^HPEG_3]I$ (**4**), were obtained by slow diffusion of a toluene/n-hexane mixture. All compounds crystallized in monoclinic or triclinic space groups.

As known from other substituted bi- and terphenyl compounds,[24] the molecular structures of all cations exhibit a torsion along the polyaryl chain, independently observable from other substituents of the salt. In some imidazolium salts, the imidazolium entity and the second phenyl ring are arranged almost co-planar with a deviation between 6° (for **2-PF$_6$**) and 17° (for **4**). Nevertheless, the putative extended, delocalized π system is reduced by a weaker overlap of the π^* orbitals. However, a plane can be defined by the imidazolium entity and the in-line located quarternary carbon atoms of the biphenyl chain as well as the linker functionality. The PEG_n substituents of the imidazolium moieties are orientated in a tortuous fashion and, therefore, prevent the common determination of the ILs' overall shape (rod-, V-, or U-shape).[14b] This non-linearity of PEG chains is well known in literature, and is explained by repulsive interactions between the oxygen electron lone pairs of neighboring ether groups.[25]

In the solid-state structure of $[BrPh_2Im^HPEG_2]I$ (**1**) (Figure 2, left), the PEG_2 substituent is not only twisted within the Im—Ph plane (see above) but also protrudes from it with an angle of 80° ($\measuredangle Im_{centroid}—N_{Im}CH_2—CH_3$). The Ph—Ph and Im—Ph torsion angles are determined to $\sim 26°$ and $\sim 23°$. Each imidazolium cation interacts with two surrounding anions via hydrogen bonding (interactions defined as the distance equal or less than the sum of the van-der-Waals radii) with distances of 2.84 Å (C(1)—H···A) and 3.02 Å (C(3)—H···A). The iodide is situated slightly shifted towards the PEG_2 chain and in front of the imidazolium ring. Hence, hydrogen bonding is also possible between one proton of the PEG_2—CH_2 (next to the imidazolium moiety) and the iodide (3.17 Å).

In the crystal packing diagram (Figure 2, bottom left), the compounds are arranged antiparallel along the crystallographic a and b axis with an inversion center (i) located between two layers. The imidazolium salts of alternating layers are shifted against each other that, exclusively, the non-directly bonded phenyl ring is lying one upon the other. However, π-π stacking of the phenyl rings with a typical distance of 3.3–3.8 Å, as reported in literature, could not be observed.[26]

$[BrPh_2Im^HPEG_3][PF_6]$ (**2-PF$_6$**) crystallizes with two independent ion pairs per unit cell. In these molecular structures (Figure 2, right), the torsion angles of the aromatic part can be determined to 31.6° (Im—Ph) and 38.4° (Ph—Ph), respectively. Similar to compound **1**, the PEG_3 substituent of **2-PF$_6$** points out of the Ph—Im plane but interacts with the imidazolium moiety via Im—O interactions due to its enhanced flexibility and chain length.[11c,25] This also justifies the larger torsion angles of **2-PF$_6$** by Ph—O repulsion compared to imidazolium salt **1**, which has a shorter PEG substituent. The "capped" arrangement of the PEG_3

Chemistry–A European Journal

Research Article
doi.org/10.1002/chem.202200100

Chemistry
Europe
European Chemical
Societies Publishing
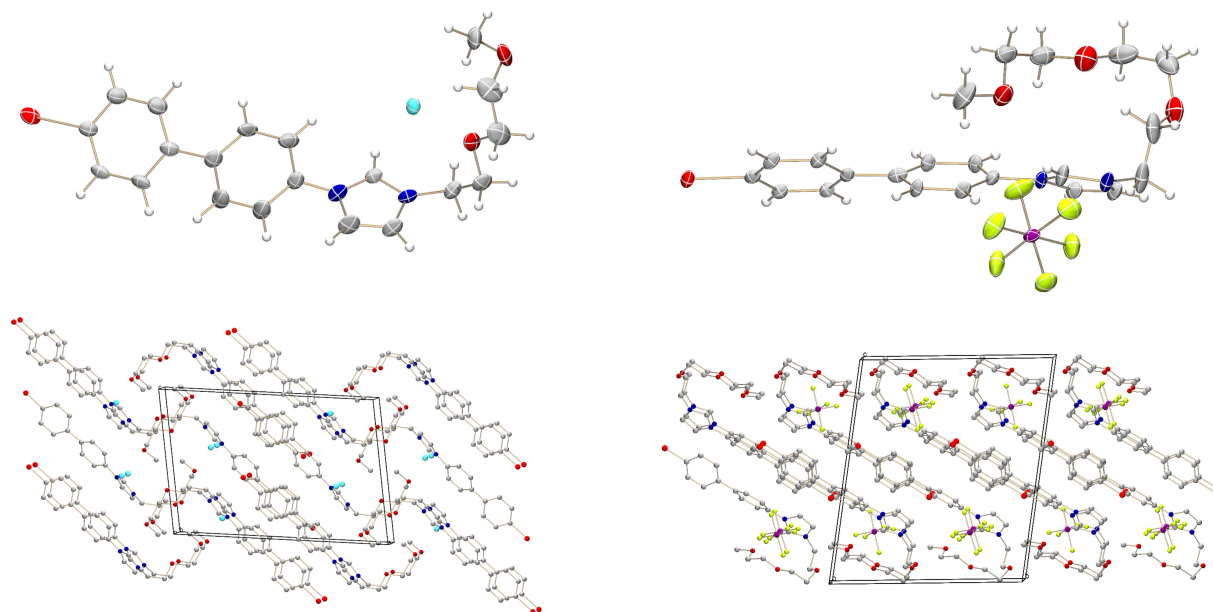
Figure 2. Solid-state molecular structures (top) and crystal packing diagrams (bottom) of [BrPh$_2$Im^{H}PEG$_2$]I (**1**) (left) and [BrPh$_2$Im^{H}PEG$_3$][PF$_6$] (**2-PF$_6$**) (right), with crystal packing diagrams viewed along the crystallographic *b* axis (for **1**) and *a* axis (for **2-PF$_6$**); color code: C – grey, H – white, N – dark blue, O – dark red; Br – red, P – dark magenta, F – green, I – cyan.

chain above the imidazolium cation prevents further interaction from this side and additionally affects the position of the anion in the crystal structure by electronic and steric repulsion. Hence, the PF$_6^-$ is situated slightly shifted downwards in front of the imidazolium entity. As observed in the crystal packing (Figure 2, bottom right), one cation interacts with two surrounding anions via hydrogen bonding of the C(1)—H (2.31 Å) and various PEG$_3$—CH$_2$ protons (2.40 Å–2.92 Å). Except the position and length of the PEG$_3$ chain, the crystal packing of **2-PF$_6$** is similar to **1**, also providing an inversion center (*i*) between alternating layers.

[BrPh$_2$Im^{H}PEG$_3$]I (**2-I**) and [EtO$_2$CPh$_2$Im^{H}PEG$_3$]I (**4**) have comparable molecular structures (Figure 3, top) and, therefore, are discussed jointly. The molecular structures of both salts show similar Ph—Ph torsion angles of 15.6° (for **2-I**) and 16.9° (for **4**) and Im—Ph torsion angles of 21.8° (for **2-I**) and 16.9° (for **4**), respectively. The PEG$_3$ chain in both compounds lies in-plane with the imidazolium moiety and partially shields the cation from the backside due to Im—O interactions.[11c] The I$^-$ counteranion of **2-I** and **4** is in-plane with the imidazolium cation situated slightly shifted towards the PEG$_3$ chain. Thus, each anion lays amidst two surrounding cations and interacts via hydrogen bonding with the C(1)—H and C(3)—H protons as well as with adjacent PEG$_3$ protons (2.92 Å–3.18 Å).

The crystal packing diagrams of **2-I** and **4** (Figure 3, bottom) distinguish in orientation of the compounds but are similar in the arrangement. The ion pairs of two successive layers (exemplified for **2-I**) are arranged parallel along the crystallographic *a* axis and rotated by 35° (41° for **4**) within the *bc* plane; thus, the PEG$_3$ chains point in the same but twist in different directions. The ion pair in the second layer is slightly shifted resulting in a visual stack of the IL's first phenyl ring.

In conclusion, the molecular structures and the crystal packing of the biphenyl and PEG$_n$-substituted imidazolium salts (**1**, **2-I**, **2-PF$_6$**, **4**) are less affected by the biphenyl-linker moiety. Unexpectedly, the length of the PEG$_n$ chain has a significant impact on the molecular structure due to possible Im—O attractive interactions as well as O—O and O – anion repulsion. The anion, however, has only a minor influence.

Thermochemical properties

The thermochemical properties, such as melting temperature (T_m), heat capacitiy (ΔC_p) as well as enthalpy (ΔH) and entropy of fusion (ΔS) were determined by DSC, and the decomposition temperature (T_d) was established by TGA. The thermochemical data of all compounds are summarized in Table 1.

The imidazolium salts **1**–**4** and **6**–**8**, as well as **10** and **11** exhibit melting temperatures in the range of 51.1–176.4 °C. However, only compounds **2-BF$_4$**, **2-PF$_6$**, **6**, **7**, and **11-PF$_6$** are genuine ILs and melt below 100 °C. The melting temperature cannot be determined for [MeSPh$_3$Im^{H}PEG$_3$]I (**9**), which decomposes before melting. In addition, polymorphism[27] can be observed for compounds **2-I** and **10** with solid-solid transitions between 54.2 and 111.8 °C. In contrast, for some imidazolium salts the crystallization process is suppressed, which often results in a supercooled liquid and, finally, in a glass transition. Notably, in [BrPh$_2$Im^{H}PEG$_3$][BF$_4$] (**2-BF$_4$**) and [HOPh$_2$Im^{H}PEG$_3$]I (**5**), this glassy state is stable over all successive cycles. For other imidazolium salts (for instance **2-PF$_6$** and **7**) a cold crystallization process is observed upon heating preceding the melting.

Remarkably, both C$_{12}$-substituted imidazolium salts [HOPh$_2$Im^{H}C$_{12}$][A] (**11-I**, **11-PF$_6$**) exhibit liquid crystalline behav-

Chemistry–A European Journal

Research Article
doi.org/10.1002/chem.202200100

Chemistry
Europe
European Chemical
Societies Publishing
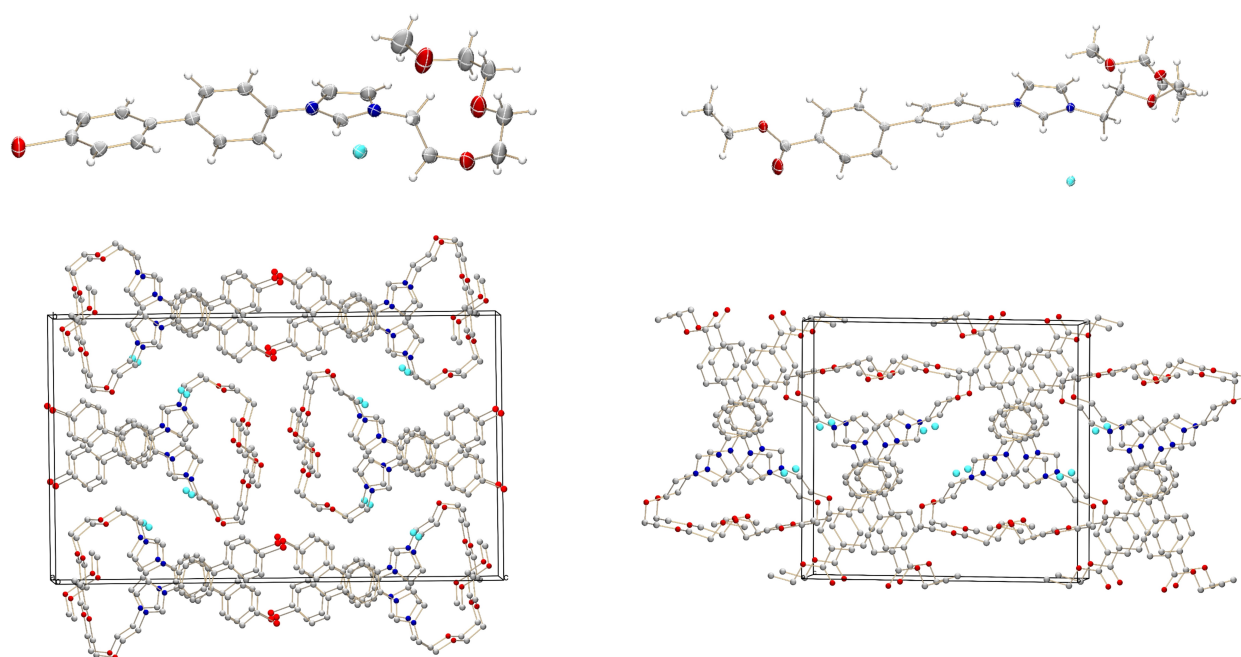
Figure 3. Solid-state molecular structures (top) and crystal packing diagrams (bottom) of [BrPh₂ImᴴPEG₃]I (**2-I**) (left) and [EtO₂CPh₂ImᴴPEG₃]I (**4**) (right) with crystal packing diagrams viewed along the crystallographic *b* axis (for **2-I**) and *c* axis (for **4**) ; color code: C – grey, H – white, N – dark blue, O – dark red; Br – red, I – cyan.

Table 1. Transition temperatures, enthalpies of fusion, entropies of fusion, and decomposition temperatures determined by DSC and TGA measurements of all asymmetrically substituted ILs **1–13**. Temperatures given below were obtained by recording the onset temperatures of the 2ⁿᵈ heating cycle; Cr = crystalline phase, I = isotropic phase, glass = glass transition, LC = liquid crystalline phase, cold cryst. = cold crystallization.

IL	Phase Transition[a]	$T_{transition}$/°C	ΔH/kJ mol⁻¹	ΔS/J mol⁻¹ K⁻¹	ΔC_p/J g⁻¹ K⁻¹	T_d/°C [a]
1	Cr–I	136.7	27.3	66.6		290.7
2-I	Cr–Cr	111.8	0.877	2.28		291.3
	Cr–I	133.1	9.91	24.4		
2-BF₄	glass – I[b]	−10.5			0.308	293.0
2-PF₆	glass – I	0.3			0.375	271.1
	cold cryst.	27.2	−17.1	−90.6		
	Cr–I	61.5	13.1	39.1		
3	glass – I	7.8			0.514	266.3
	cold cryst.	72.7	−33.0	−95.4		
	Cr–I	140.0	32.4	78.4		
4	cold cryst.	57.3	−22.4	−67.8		277.5
	Cr–I	107.3	27.3	71.8		
5	glass – I	9.4			0.307	271.3
6	glass – I	−21.7			0.294	293.6
	Cr–I	75.9	5.59	16.0		
7	glass – I	−5.4			0.504	278.2
	cold cryst.	30.8	−11.5	−37.8		
	Cr–I	51.5	8.84	27.2		
8	Cr–LC	111.5	16.6	43.1		273.6
	LC–I	127.8	1.91	4.77		
9	–	–	–	–	–	281.7
10	Cr–Cr	54.2	8.29	25.3		279.3
	Cr–I	176.4	32.8	72.9		
11-I	Cr–LC	114.8	15.8	40.6		294.4
	LC–LC′	165.9	5.61	12.8		
	LC′–I	187.7	3.05	6.63		
11-PF₆	Cr–LC	98.9	15.8	42.5		n.d.[c]
	LC–LC	149.9	4.39	10.2		
	LC′–I	174.6	2.12	4.73		

[a] DSC and TGA traces of all compounds can be found in the Supporting Information (Figure S7–16). [b] [BrPh₂ImᴴPEG₃][BF₄] (**2-BF₄**) melts at 58.8 °C (ΔH = 14.9 kJ mol⁻¹) during the first heating period and remains in the glassy state during the successive cycles. [c] because of HF formation and subsequent damage to the thermocouple, thermal stability was not determined for fluorine containing compounds.

Chemistry–A European Journal

Research Article
doi.org/10.1002/chem.202200100

Chemistry Europe
European Chemical
Societies Publishing

ior, possessing two types of liquid crystalline phases. For the PEG$_3$-substituted analogue **5**, a mesophase cannot be observed. **11-I** shows a solid-mesophase transition at 114.8 °C ($\Delta H =$ 15.8 kJ mol^{-1}). The second phase transition occurs at 165.9 °C ($\Delta H = 5.61$ kJ mol^{-1}), the clearing temperature of **11-I** was observed at 187.7 °C ($\Delta H = 3.05$ kJ mol^{-1}). Similar liquid crystalline behavior was obtained for **11-PF$_6$**, with transition temperatures ~16 °C lower than those determined for the corresponding iodide salt. The liquid crystalline behavior of [HOPh$_2$Im^{H}R][A] confirms the predication of Kouwer and co-workers[16] that, at least, one long alkyl chain has to be N- and/or O-substituted for this type of imidazolium-based ILCs. In addition, the terphenyl-substituted compound [EtO$_2$CPh$_3$Im^{H}PEG$_3$]I (**8**) shows liquid crystalline behavior, possessing its solid-mesophase transition at 111.5 °C ($\Delta H = 16.6$ kJ mol^{-1}) and its clearing temperature at 127.8 °C ($\Delta H = 1.91$ kJ mol^{-1}).

Generally, the melting temperature of the imidazolium salts, presented herein, is dependent on the chain length of both the aryl and the alkyl substituent as well as on the counteranion. The melting temperature increases with longer aryl substituents (Ph$_2$ < Ph$_3$); however, with increasing length of the PEG$_n$ substituent, the melting temperature decreases. Moreover, and due to enhanced van-der-Waals interactions of the side chain, the C$_{12}$-substituted imidazolium salts offer higher melting temperatures than the PEG$_n$-substituted ones. Comparing the melting points within the series of different anions, the temperature unexpectedly increases in the following order: [PF$_6$]$^-$ < I$^-$ < [BF$_4$]$^-$. A possible explanation might be the anion position within the solid imidazolium salt. Due to the "capped" arrangement of the PEG$_3$ chain in **2-PF$_6$** above the imidazolium, the [PF$_6$]$^-$ anion is displaced and the cation anion interaction is attenuated. Contrasting, the I$^-$ salt is not displaced, since the PEG$_3$ chain interacts with the imidazolium moiety from the backside; thus, the cation-anion distance remains shorter.

The decomposition temperature of the imidazolium salts reported herein were determined to be between 266 and 294 °C; hence, within a range of 24 °C. As expected for asymmetrically substituted ILs, a multi-stage decomposition is observed for all imidazolium salts with a residual mass of up to 30 %. Remarkably, and in contrast to literature,[28] neither the anion nor the constitution of the cation, i.a. the type or length of the N-aryl and N′-alkyl substituent, has a notable impact on the thermal stability. Regardless, the terphenyl-substituted imidazolium salts show tendency to decompose at lower temperatures compared to the biphenyl-substituted salts. The decomposition temperature in this series of imidazolium salts is mainly depending on the aromatic substituent at *para*-position, and increases as follows: HO− < NC− < EtO$_2$C− < Br− < MeS−.

N-Diaryl N′-alkyl substituted N-heterocyclic carbene complexes of mono- and divalent transition metals

Synthesis

The NHC complexes reported herein comprise the transition metals Mn^{II} (**12**), Fe^{II} (**13**), Co^{II} (**14, 15**), Ni^{II} (**16**), Zn^{II} (**17**), Cu^I (**18**), Ag^I (**19**), Au^I (**20**), and were synthesized starting from [LPh$_2$Im^{H}R]I (L = Br, CN; R = PEG$_n$, C$_{12}$H$_{25}$; n = 2, 3) (**1–3, 10**) (Scheme 2).

The imidazolium C(1)−H position of the respective salt was deprotonated by potassium hexamethyldisilazide, KN(SiMe$_3$)$_2$, in THF; the resulting precipitate was filtered off and added to a suspension of the respective metal halide in THF. Alternatively, all divalent metal complexes **12–17** can be synthesized via transmetallation of the Ag^I NHC complex with the desired metal(II) halide in dichloromethane. Complexes **12–20** were characterized by *CHN* elemental combustion analysis, ^{1}H and ^{13}C NMR spectroscopy. The paramagnetic complexes **12–15** were further studied by SQUID magnetometry as well as X-band EPR and ^{57}Fe Mössbauer spectroscopy, where appropriate.

Solid-state molecular structures

Crystals of **12–17** and **19**, suitable for SC-XRD analysis, were obtained via vapor diffusion of either tetrahydrofuran/*n*-pentane or dichloromethane/diethyl ether. All complexes crystallize in the triclinic space group $P\bar{1}$ (for details see Supporting Information).

For this type of complex, three coordination geometries are obtained: linear, square planar, and tetrahedral. The solid-state molecular structure of **19** (Figure 4, left) shows the coordination of two BrPh$_2$ImPEG$_3$ carbene ligands to a Ag^I center, resulting in the linear, coordinatively saturated, cationic *bis*-NHC complex **19**; a complex [AgCl$_2$]$^-$ entity forms the counteranion. This type of molecular structure is well-known in the literature.[29] Unexpectedly, both carbene ligands are arranged in a bent
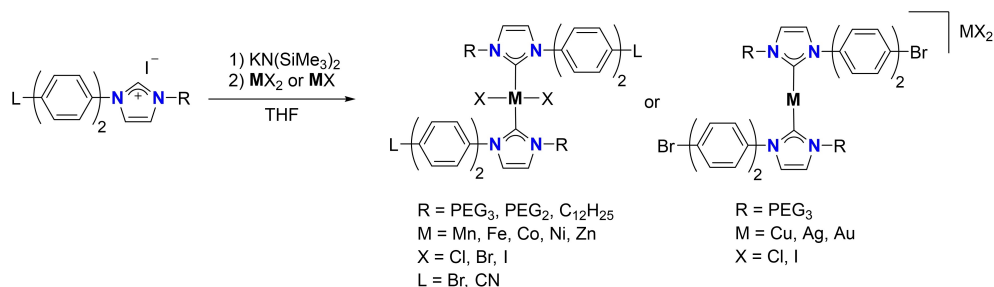
Scheme 2. General synthetic pathway of mono- and divalent transition metal-NHC complexes.

Chemistry–A European Journal

Research Article
doi.org/10.1002/chem.202200100

Chemistry Europe
European Chemical
Societies Publishing

M = Ag (**19**), linear   M = Ni (**16**), square planar   M = Zn (**17**), tetrahedral
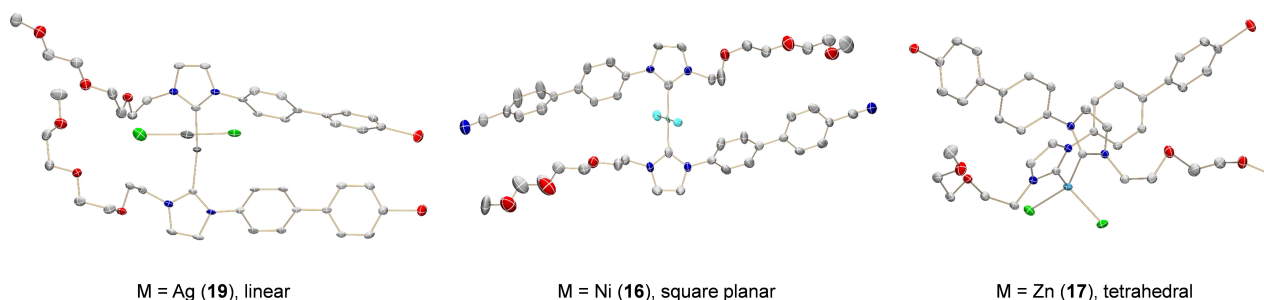
Figure 4. Solid-state molecular structures of [(BrPh$_2$Im^{H}PEG$_3$)$_2$Ag][AgCl$_2$] (**19**) (left), [(NCPh$_2$ImPEG$_3$)$_2$NiI$_2$] (**16**) (middle) and [(BrPh$_2$ImPEG$_2$)$_2$ZnCl$_2$] (**17**) (right), exemplified for all tetrahedrally coordinated transition metal complexes Mn^{II} (**12**), Fe^{II} (**13**), and Co^{II} (**14**, **15**), (see Supporting Information). Hydrogen atoms and co-crystallized solvent are omitted for clarity; color code: C – grey, N – dark blue, O – dark red, Cl – light green, Br – red, I – cyan, Ag – dark grey, Ni – green, Zn – turquoise.

fashion with an angle ∢C$_{carbene}$–Ag–C$_{carbene}$ of 170.9(2)°. This might be due to electronic and steric repulsive interactions between the aryl substituent. The imidazolylidene moieties are close to coplanar with a deviation of 10°. The additional repulsion of each PEG$_3$ and aryl substituents might also explain the slightly elongated Ag–C$_{carbene}$ distance of 2.100(4) Å and 2.104(4) Å compared to literature-reported values ($d_{av,lit.}$(Ag–C$_{carbene}$) = 2.081 Å).[30] The close-to-linear [AgCl$_2$]$^-$ anion (∢Cl–Ag–Cl = 174.03(4)°) is associated through Ag···Ag interaction with a Ag–Ag distance of 3.1364(5) Å.[31] The average Ag–Cl bond length is 2.336(2) Å.

As often reported for *bis*-NHC Ni^{II} dihalide complexes,[32] the Ni^{II} center in [(NCPh$_2$ImPEG$_3$)$_2$NiI$_2$] (**16**) (Figure 4, middle) is coordinated in a square planar geometry. Both carbene and iodido ligands are bound mutually *trans* to each other with the PEG$_3$ substituents pointing in opposite directions and near linear ∢C$_{carbene}$–Ni–C$_{carbene}$ and ∢I–Ni–I angles of 177.4(3)° and 178.6(2)°, respectively. The imidazolylidene entities are arranged close to coplanar (deviation of 10°). The average Ni–C and Ni–I bond distances of 1.919(8) Å and 2.490(6) Å are in accord with literature-reported values.[33]

Bis-NHC complexes of mid to late first-row transition metals, can be used as catalyst for various organic reactions.[34] However, molecular structures of the [(NHC)$_2$MX$_2$]-type (M = Mn, Fe, Co; X = halides), predominantly for Mn^{II} and Co^{II}, are rather rare; for Zn^{II} we here report, to the best of our knowledge, the first solid-state molecular structure. The lack of molecular structures of such complexes might be due to the possible dimerization to [(NHC)$_2$X$_2$(μ-X)$_2$M$_2$] (X = halide).[35] In the solid-state structure of [(BrPh$_2$ImR)$_2$MX$_2$]-type (M = Mn, Fe, Co, Zn) complexes (Figure 4, right) the metal center is coordinated in a

distorted tetrahedral fashion; the PEG$_n$ chains point in opposite directions, likely due to steric and electronic repulsion.

In order to study the influence of the NHC's side chains, an exchange of the PEG$_3$ moieties in the Co^{II} complex **14** by dodecyl substituents was implemented. In contrast to the PEG$_n$-substituted NHC complexes – with almost equal ∢C$_{carbene}$–M–C$_{carbene}$ and ∢X–M–X angles (max. difference of 5°) – the C$_{12}$-substituted one shows a significant distortion of the tetrahedron (∢C$_{carbene}$–Co–C$_{carbene}$ = 121.1(2)°, ∢(Br–Co–Br) = 110.42(2)°). Selected values of structural parameters are summarized in Table 2. For complexes **12–15** and **17** bond lengths and angles are in good agreement with reported literature values.[35a,36] However, in the molecular structure of **13**, the observed Fe–C$_{carbene}$ bond (2.128(3) Å) is slightly shorter compared to other known *bis*-NHC iron(II) halide complexes ($d_{av,lit.}$(Fe–C$_{carbene}$) = 2.149 Å).[37]

NMR spectroscopy of the diamagnetic bis-NHC complexes 16–20

Because of the complexes' C_2 symmetry, the ^{1}H NMR spectra of complexes **16–20** (Figure S2–S6) show a set of signals for one carbene ligand. In the aromatic region, the biphenyl substituents give rise to 4 doublets between 7.88 and 7.37 ppm, whereas 2 doublets between 7.55 and 7.11 ppm can be assigned to the backbone protons of the imidazolylidene moiety. Additionally, a characteristic signal pattern for the PEG$_n$ substituents can be observed in the aliphatic region, consisting of 2 *pseudo*-triplets, 1 singlet and various multiplets. The lack of a signal for C(1)–H as well as signals between 170–185 ppm for

Table 2. Selected structural parameters, bond lengths [Å] and angles [°] for complexes **12–15** and **17**.

[(BrPh$_2$ImR)$_2$MX$_2$]	Mn^{II}, R = PEG$_2$ (**12**)	Fe^{II}, R = PEG$_2$ (**13**)	Co^{II}, R = PEG$_3$ (**14**)	Co^{II}, R = C$_{12}$ (**15**)	Zn^{II}, R = PEG$_2$ (**17**)
d_{av} (M–C$_{carbene}$)	2.206(3) Å	2.126(3) Å	2.061(6) Å	2.062(3) Å	2.064(2) Å
d_{av} (M–X)	2.366(2) Å	2.3072(9) Å	2.4245(2) Å	2.4302(7) Å	2.3160(4) Å
∢(C$_{carbene}$–M–C$_{carbene}$)	111.6(2)°	108.7(2)°	111.2(2)°	121.1(2)°	113.51(6)°
∢$_{av}$ (C$_{carbene}$–M–X)	109.7(1)°	108.74(8)°	110.2(2)°	106.3(2)°	109.89(4)°
∢(X–M–X)	106.28(4)°	107.66(3)°	104.92(4)°	110.42(2)°	103.39(2)°

X is defined as halide.

Chemistry–A European Journal

Research Article
doi.org/10.1002/chem.202200100

Chemistry Europe
European Chemical
Societies Publishing

the C(1) atom in the ^{13}C NMR spectra indicates a successful coordination to the metal center. Signals in the ^{1}H NMR spectra for both protons of the imidazolylidene backbone and the biphenyl moiety are upfield-shifted compared to the ^{1}H NMR spectra of the related imidazolium salt due to the omission of the positive charge and the increased electron density in the imidazolylidene entity. In case of the monovalent NHC complexes, this phenomenon is also observed for the protons of the directly bonded CH_2 groups in the PEG chain.

Magnetism of the bis-NHC Mn^{II} 12

As expected, the Mn^{II} complex **12** possesses an $S = 5/2$ ground state for a tetrahedrally coordinated high-spin d^5 metal center, experimentally confirmed by EPR spectroscopy at low temperature and SQUID magnetization measurements. The X-band EPR spectrum at 96 K (Figure 6, left) shows a broad, rhombic signal, simulated to $g_1 = 2.11$, $g_2 = 2.01$, and $g_3 = 1.88$. Hyperfine coupling to the ^{55}Mn nucleus ($I = 5/2$, 100%) is well resolved, with a coupling constant simulated to $A_2 = 233$ MHz. Temperature-dependent SQUID magnetometry of **12** (Figure 5, right, blue trace) exhibits an effective magnetic moment of 5.80 μ_B at room temperature ($\mu_{eff}^{s.o.} = 5.92$ μ_B). Upon cooling, the moment remains constant until 55 K. Simulation of the temperature-dependent VTVF susceptibility data reveals a zero-field splitting parameter, $|D|$, of 0.8 cm^{-1}, rhombicity, E/D, of 0.16 and an average g-value of 2.0, as expected for a d^5, $S = 5/2$ spin system.

Magnetism of the bis-NHC Fe^{II} 13

The zero-field ^{57}Fe Mössbauer spectrum of complex **13** (Figure 5, left), recorded at 77 K on a solid sample, features a quadrupole doublet with a quadrupole splitting, ΔE_Q, of 3.59 mm s^{-1}, and an isomer shift, δ, of 0.80 mm s^{-1}, characteristic for a high-spin Fe^{II} complex with an $S = 2$ ground state. This is confirmed by susceptibility measurements of **13** (Figure 5, right, red trace) with an effective magnetic moment of 4.97 μ_B at room temperature ($\mu_{eff}^{s.o.} = 4.90$ μ_B). The average g-value of 2.03 as well as the zero-field splitting parameter, $|D|$, of 7.24 cm^{-1}

and the remarkable high rhombicity, E/D, of 0.33 can be determined by global simulation of the data.

Magnetism of the bis-NHC Co^{II} 14

The EPR spectrum of **14** (Figure 6, right) exhibits a rhombic signal with effective g-values of $g_1 = 4.65$, $g_2 = 2.80$, and $g_3 = 2.70$ at 7 K, which indicates an $S = 3/2$ ground state for a high-spin d^7 metal center. Hyperfine-coupling to the ^{59}Co metal center (100%, $I = 7/2$) is well resolved as an octet pattern with a coupling constant of $A_2 = 704$ MHz observed on the central g-value. The quartet ground state of **14** is also verified by susceptibility measurements (Figure 5, right, green trace) that exhibit an effective magnetic moment, μ_{eff}, of 4.29 μ_B at room temperature. Because of spin-orbit coupling, this moment deviates significantly from the spin-only value calculated for an $S = 3/2$ spin system ($\mu_{eff}^{s.o.} = 3.87$ μ_B), which is often observed in divalent cobalt complexes.[36a,38] Simulations of the magnetization data give an average g-value of 2.21, a zero-field splitting parameter, $|D|$, of 7.26 cm^{-1} as well as a rhombic contribution of electron density ($E/D \approx 0.23$).

Molecular titanium-phenolate complexes as models for Ti-supported imidazolium salts and their corresponding NHC complexes

In order to improve the possibilities of chemical and structural analysis of surface-immobilized ILs and their corresponding transition metal complexes, a structural motif was developed. This model system, consisting of a Ti(IV) center and [HOPh$_2$Im^{H}C$_{12}$]$^+$ (**11**) and its respective bis-NHC Fe complex, coordinated via its linker moiety, provides both a molecular example for ease of characterization and a mimic of a potential electro-active surface (e.g. TiO$_2$).
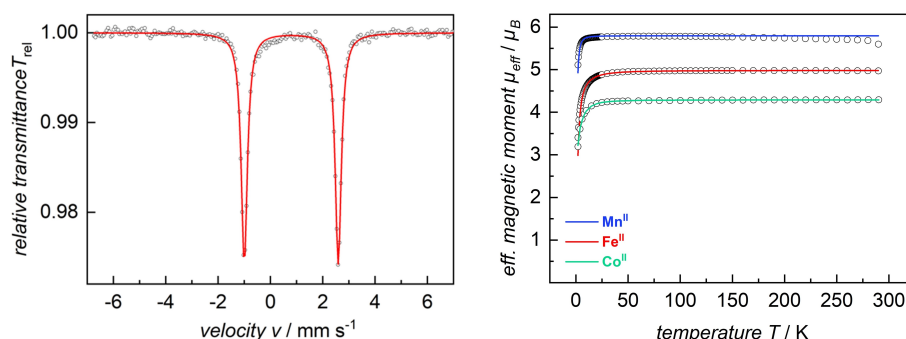
Figure 5. Zero-field ^{57}Fe Mössbauer spectrum of **13** (left) and SQUID magnetization measurements of microcrystalline solid samples (right) of **12** (blue trace), **13** (red trace), and **14** (green trace). The solid lines represent the best global fits for $S = 5/2$ (**12**, $\mu_{eff,RT} = 5.80$ μ_B), $S = 2$ (**13**, $\mu_{eff,RT} = 4.90$ μ_B), and $S = 3/2$ (**14**, $\mu_{eff,RT} = 4.29$ μ_B) spin systems (right) and ^{57}Fe Mössbauer simulation parameters for **13** of $\delta = 0.80$ mm s^{-1}, $\Delta E_Q = 3.59$ mm s^{-1}, and $\Gamma_{FWHM} = 0.28$ mm s^{-1} (left).

Chemistry–A European Journal

Research Article
doi.org/10.1002/chem.202200100

Chemistry Europe
European Chemical
Societies Publishing
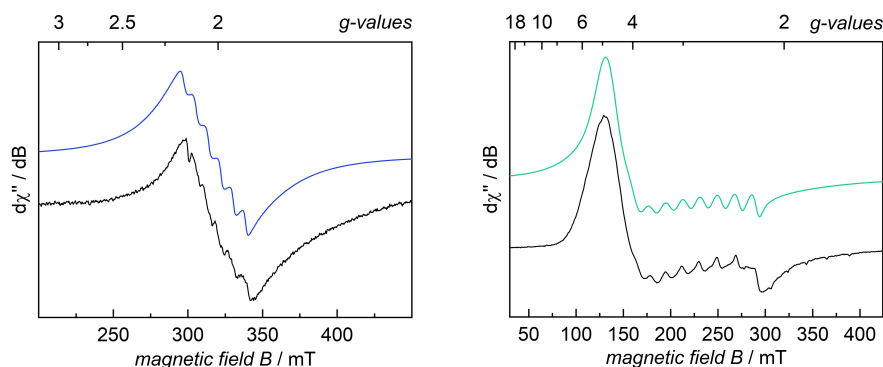
Figure 6. X-band EPR spectra of the *bis*-NHC Mn^{II} (**12**, left, blue) and Co^{II} (**14**, right, green) complexes, measured at 96 K (for **12**) and 7 K (for **14**), in frozen THF solution (10 mM). Colored lines represent simulations for $S = 5/2$ (**12**) and $S = 3/2$ (**14**) with simulation parameters of $g_1 = 2.11$, $g_2 = 2.01$, $g_3 = 1.67$, $W_1 = 37.9$ mT, $W_2 = 1.51$ mT, $W_3 = 55.6$ mT, $A_2 = 233$ MHz for **12** and $g_1 = 4.65$, $g_2 = 2.80$, $g_3 = 2.70$, $W_1 = 18.1$ mT, $W_2 = 6.01$ mT, $W_3 = 80.0$ mT, $A_2 = 704$ MHz for **14**.
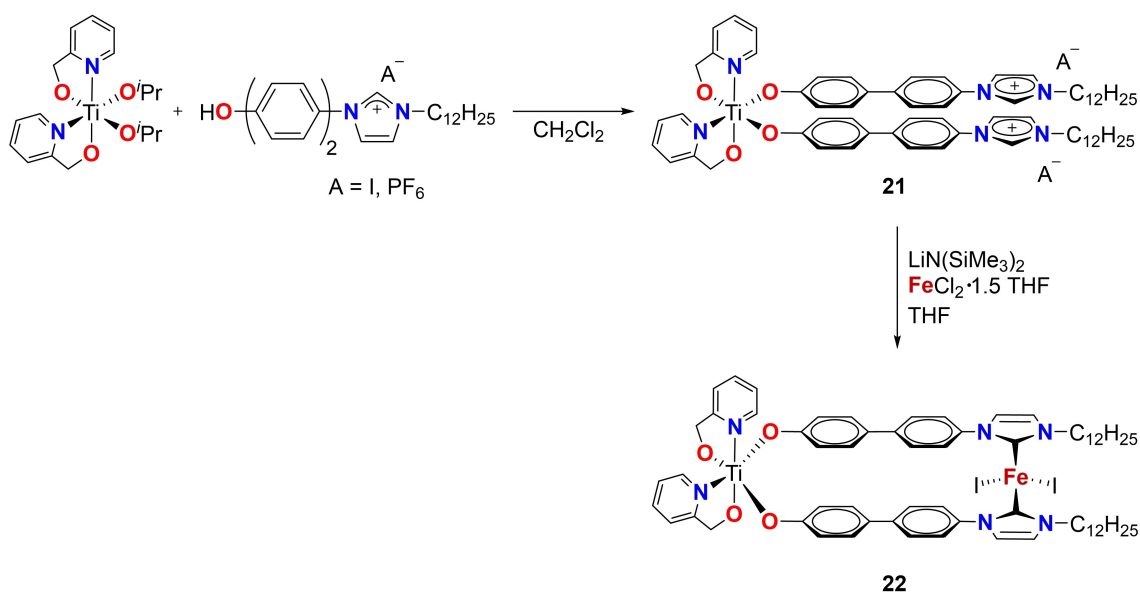
Scheme 3. Synthetic route to complexes **21** and **22**.

Synthesis

Starting from the [HOPh$_2$Im^{H}C$_{12}$]I salt (**11-I**), the hydroxy linkers of two IL cations can be coordinated to the precursor complex [(OPy)$_2$Ti(O^{i}Pr)$_2$] (OPy = pyridin-2-ylmethanolate); thereby, exchanging both *iso*-propoxides by the imidazolium salt's phenolate moieties (Scheme 3). Subsequently, the resulting complex [(OPy)$_2$Ti(OPh$_2$Im^{H}C$_{12}$)$_2$]I$_2$ (**21-I**) can be coordinated to FeCl$_2$ via deprotonation of the imidazolium unit with lithium hexamethyldisilazide, LiN(SiMe$_3$)$_2$, in tetrahydrofuran. Finally, the addition of the Fe precursor yields the heterodinuclear target complex [(OPy)$_2$Ti(OPh$_2$Im^{H}C$_{12}$)$_2$(FeI$_2$)] (**22**). In **22**, the Ti ion is situated in an octahedral N$_2$O$_4$ coordination environment, whereas the tetrahedral Fe ion is bound to two NHCs and the remaining two halides. Anion exchange of **21-I** is proceeded by either using different anions of the starting compound **11** or an anion metathesis of **21-I** using the corresponding silver salt in dichloromethane.

The complexes **21** and **22** were characterized by *CHN* elemental combustion analysis and NMR spectroscopy. The paramagnetic Fe^{II} complex **22** was further studied by SQUID magnetometry as well as ^{57}Fe Mössbauer spectroscopy.

Spectroscopic characterization of [(OPy)$_2$Ti(OPh$_2$Im^{H}C$_{12}$)$_2$](PF$_6$)$_2$ (21-PF$_6$)

The ^{1}H NMR spectrum of **21-PF$_6$** (Figure 7) features signals exclusively in the diamagnetic region that confirms the expected non-magnetic ($S = 0$) ground state for Ti(IV) in complex **21** in solution. Because of the C_2 symmetry of **21**, only 1 set of signals for each pyridin-2-ylmethanolate and imidazolium ligand can be observed. Each proton can be unambigu-

Chemistry–A European Journal

Research Article
doi.org/10.1002/chem.202200100

**Chemistry
Europe**

European Chemical
Societies Publishing
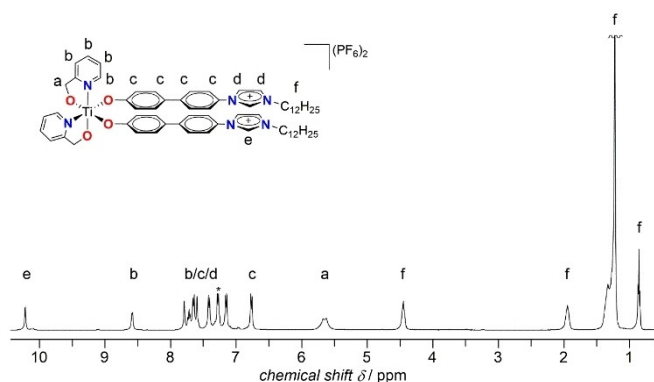
Figure 7. ^{1}H NMR spectrum of [(OPy)$_2$Ti(OPh$_2$Im^{H}C$_{12}$)$_2$](PF$_6$)$_2$ (**21-PF$_6$**), measured in chloroform-d_1 at 400 MHz at room temperature. Solvent residual signals are marked with an asterisk (*).

ously identified and assigned by integration. The dodecyl substituents of the imidazolium entities give rise to 4 signals in the aliphatic region, including 2 characteristic *pseudo* triplets at 4.43 and 0.84 ppm as well as a *pseudo* quintet at 1.93 ppm. In the aromatic region, four doublets and two singlets between 7.78 and 6.74 ppm are unequivocally assigned to the biphenyl substituent as well as to the backbone of the imidazolium ligand, respectively. The singlet at 10.20 ppm of the C(1)–H indicates an unimpaired, positively charged imidazolium entity. Signals related to the pyridine ligand can be observed at 8.57 ppm (doublet) and 7.71 ppm (triplet). The expected third and fourth proton arise as a multiplet between 7.27 and 7.24 ppm, which is superimposed by the residual solvent signal of chloroform-d_1. The methylene protons of the deprotonated pyridin-2-ylmethanolate ligand give rise to a broad doublet at 5.67 ppm (established by a combination of, ^{1}H-^{1}H COSY, ^{13}C and ^{1}H-^{13}C HMQC). Additionally, variable temperature NMR measurements reveal their diastereotopic nature by splitting the coalescent signal at lower temperatures to a well-resolved AB system (Figure S1).

The UV/Vis electronic absorption spectrum of complex **21-PF$_6$** shows two intense bands at $\lambda = 227$ nm and 302 nm (Figure S18, left). The highest energy band at 227 nm exhibits

an extinction coefficient of $\varepsilon = 56750$ M^{-1} cm^{-1} and can be assigned to a π-π* transition of the pyridin-2-ylmethanolate ligand, whereas the broad band at 302 nm ($\varepsilon = 43600$ M^{-1} cm^{-1}) is related to a LMCT transition of the imidazoliums' phenolate linker to the Ti center.[39]

Spectroscopic and magnetic characterization of [(OPy)$_2$Ti(OPh$_2$ImC$_{12}$)$_2$(FeI$_2$)] (22)

Upon coordination to iron, the UV/Vis electronic absorption spectrum of **22** (Figure S18, right) retains the bands at 228 nm (81980 M^{-1} cm^{-1}) and 297 nm (51990 M^{-1} cm^{-1}). This similarity to complex **21** indicates the preserved coordination of the phenolate linker to the titanium center, also confirmed by the lack of an OH stretching vibration around 3200 cm^{-1} in the IR vibrational spectrum of **22** (Figure S19, right).

The solid-state ^{57}Fe Mössbauer spectrum of **22** (Figure 8, left), recorded at 77 K, exhibits a single quadrupole doublet with an isomer shift, δ, of 0.77 mm s^{-1} and quadrupole splitting, ΔE_Q, of 3.08 mm s^{-1}. Susceptibility measurements of complex **22** feature an effective magnetic moment of 5.1 μ_B at 300 K, which is slightly higher than the spin-only value ($\mu_{eff}^{s.o.} = 4.9$ μ_B) due to spin-orbit coupling. Simulation of the SQUID data (Figure 8, right) revealed the zero-field spitting parameter $|D| = 9.7$ cm^{-1}, a remarkable rhombicity ($E/D = 0.28$) as well as an average g-value of 2.09. Both methods show characteristic parameters for a well-isolated high-spin Fe^{II} complex ($S = 2$) that suggested an electronical and structural similarity to the *bis*-NHC Fe^{II} complex **13** ($\delta = 0.80$ mm s^{-1}, $\Delta E_Q = 3.59$ mm s^{-1}).

Electrochemical studies

Cyclic voltammetry (CV) and linear sweep voltammetry (LSV) (Figure 9, Figure S26) of complex **21-I** were conducted in order to investigate possible redox processes of the complex. The CV, measured in acetonitrile with [Fe(Cp)$_2$]$^{+/0}$ as internal standard, shows three quasi-reversible redox events at −1.85 V, −0.18 V, and 0.25 V. At −0.18 V, and 0.25 V, both iodide counter anions of the complex are oxidized in a four- and two-electron step,
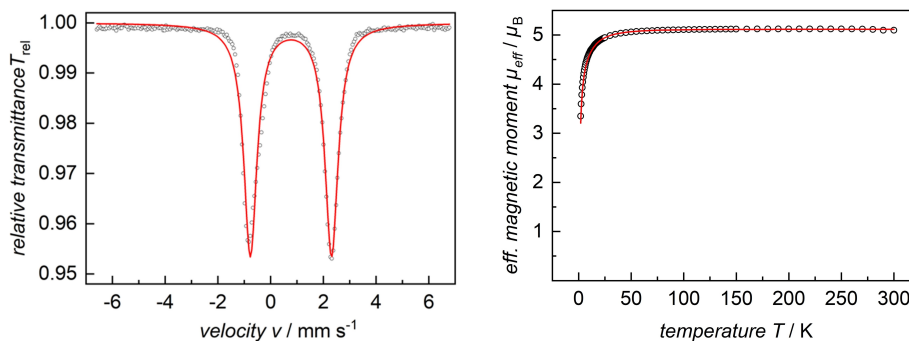
Figure 8. Zero-field ^{57}Fe Mössbauer spectrum of **22** (left), recorded in solid state at 77 K, and SQUID magnetization measurement of a microcrystalline solid sample (right, $\mu_{eff,RT} = 5.10$ μ_B) of complex **22**. The red lines represent the best global fit with ^{57}Fe Mössbauer simulation parameters of $\delta = 0.77$ mm s^{-1}, $\Delta E_Q = 3.08$ mm s^{-1}, and $\Gamma_{FWHM} = 0.60$ mm s^{-1}.

Chemistry–A European Journal

Research Article
doi.org/10.1002/chem.202200100

Chemistry Europe
European Chemical
Societies Publishing
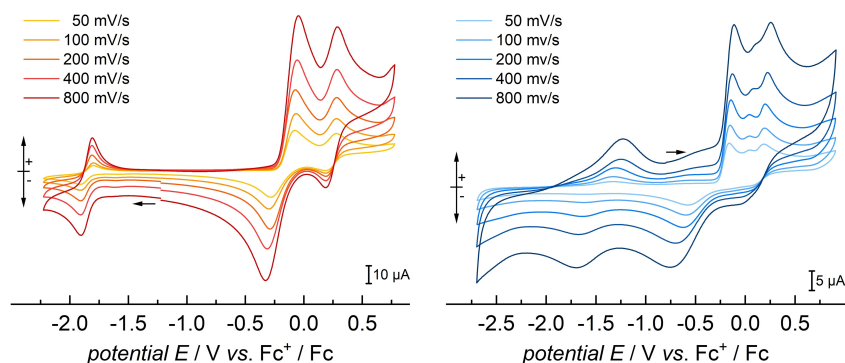
Figure 9. Cyclic voltammograms of complexes **21-I** (left) and **22** (right), measured at room temperature in acetonitrile (for **21-I**) and THF/acetonitrile (for **22**) solution with 0.1 M N(n-Bu)$_4$PF$_6$ electrolyte and varying scan rates, referenced vs. [Fe(Cp)$_2$]$^{+/0}$.

respectively.[40] The redox event at −1.85 V occurs as a one-electron reduction and can be assigned to a Ti$^{4+/3+}$ redox pair.

The CV of **22** show multiple redox transitions of complex nature. Hence, their assignment is challenging and needs to be further studied.

Conclusion

Herein, we present a scalable synthetic route to asymmetric N-polyaryl and N'-alkyl substituted imidazolium salts that is independent from the polyaryl chain length and suitable for most types of aryl substituents. These imidazolium salts, namely [LPh$_m$Im^{H}R][A] (m = 2, 3; R = PEG$_n$, C$_{12}$H$_{25}$; n = 2, 3; A = anion) (1-11), with a linker moiety for potential surface adsorption, show characteristic thermal properties, such as polymorphism and glass transitions. Additionally, some imidazolium salts (**8**, **11-I**, **11-PF$_6$**) show liquid crystalline behavior suitable for application for example in dye-sensitized solar cells or as templates for the synthesis of nanomaterials or mesoporous materials.[17,41] However, the transition to the mesophase occurs at relatively high temperatures, which may limit their application. The decomposition temperatures of the imidazolium salts **1**–**11** can be observed between 266 and 294 °C, mainly depending on the para-substituent of the aryl chain. Contrasting, the molecular structure of these types of imidazolium salts, studied by **1**, **2-I**, **2-PF$_6$**, and **4**, is mainly influenced by the length of the PEG$_n$ substituent. Due to electronic O···O repulsive and Im···O attractive interactions, for example the twisted PEG$_3$ chain can arrange protectively above or behind the imidazolium entity and influence the position of the anion, the torsion angle of the biphenyl moiety as well as the arrangement within the crystal packing.

On the basis of these imidazolium salts, a series of first-row transition metal and group 11 metal bis-NHC complexes were presented. These complexes are based on [BrPh$_2$Im^{H}PEG$_n$]I and [NCPh$_2$Im^{H}PEG$_3$]I salts as carbene precursors and include the divalent transition metals Mn^{II}, Fe^{II}, Co^{II}, Ni^{II}, and Zn^{II} (complexes **12**–**17**) as well as the monovalent group 11 metals Cu^{I}, Ag^{I}, and Au^{I} (complexes **18**–**20**). These complexes coordinate in 3 different geometries: linear (Ag^{I}), square planar (Ni^{II}) and

distorted tetrahedral (Mn^{II}, Fe^{II}, Co^{II}, Zn^{II}). The arrangement of the ligands and the degree of distortion is mainly affected by the nature of the aliphatic carbene substituents. The transition metal complexes **12**–**20** show typical parameters regarding their magnetic and spectroscopic characterization.

In addition, the complexes [(OPy)$_2$Ti(OPh$_2$Im^{H}C$_{12}$)$_2$]A$_2$ (**21**, A = I$^-$, PF$_6^-$) and [(OPy)$_2$Ti(OPh$_2$ImC$_{12}$)$_2$FeI$_2$] (**22**) were developed as a homogeneous model system for surface adsorbed ILs. Despite the lack of an X-ray crystal structure determination, complexes **21** could be clearly identified by the assignment of signals in the NMR spectroscopic characterization. The titanium-bridged Fe^{II} bis-NHC complex **22**, however, shows characteristic parameters in ^{57}Fe Mössbauer spectroscopy and SQUID magnetization data.

Deposition Numbers CCDC-2122936 (for **1**), CCDC-2122937 (for **2-I**), CCDC-2122938 (for **2-PF$_6$**), CCDC-2122939 (for **4**), CCDC-2122940 (for **12**), CCDC-2122941 (for **13**), CCDC-2122942 (for **14**) CCDC-2122943 (for **15**), CCDC-2122944 (for **16**), CCDC-2122945 (for **17**), and CCDC-2122946 (for **19**) contain the supplementary crystallographic data for this paper. These data are provided free of charge by the joint Cambridge Crystallographic Data Centre and Fachinformationszentrum Karlsruhe Access Structures service.

Conflict of Interest

The authors declare no conflict of interest.

Data Availability Statement

The data that support the findings of this study are available in the supplementary material of this article.

[1] P. Wasserscheid, W. Keim, *Angew. Chem. Int. Ed.* **2000**, *39*, 3772–3789; *Angew. Chem.* **2000**, *112*, 3926–3945.

[2] J. S. Wilkes, P. Wasserscheid, T. Welton, in *Ionic Liquids in Synthesis*, (Eds.: P. Wasserscheid, T. Welton), Wiley-VCH, Weinheim, **2008**.

[3] a) X. Wang, M. Sternberg, F. T. U. Kohler, B. U. Melcher, P. Wasserscheid, K. Meyer, *RSC Adv.* **2014**, *4*, 12476–12481; b) C. M. Gordon, J. D. Holbrey, A. R. Kennedya, K. R. Seddon, *J. Mater. Chem.* **1998**, *8*, 2627–2636; c) C. J. Bradaric, A. Downard, C. Kennedy, A. J. Robertson, Y. Zhou, *Green Chem.* **2003**, *5*, 143–152; d) K. Lava, K. Binnemans, T. Cardinaels, *J. Phys. Chem. B* **2009**, *113*, 9506–9511; e) K. Goossens, K. Lava, P. Nockemann, K. Van Hecke, L. Van Meervelt, K. Driesen, C. Gorller-Walrand, K. Binne-mans, T. Cardinaels, *Chem. Eur. J.* **2009**, *15*, 656–674.

[4] N. V. Plechkova, K. R. Seddon, *Chem. Soc. Rev.* **2007**, *37*, 123–150.

[5] S. Lee, *Chem. Commun.* **2006**, 1049–1063.

[6] P. Nockemann, B. Thijs, S. Pittois, J. Thoen, C. Glorieux, K. Van Hecke, L. Van Meervelt, B. Kirchner, K. Binnemans, *J. Phys. Chem. B* **2006**, *110*, 20978–20992.

[7] E. D. Bates, R. D. Mayton, I. Ntai, J. H. Davis Jr., *J. Am. Chem. Soc.* **2002**, *124*, 926–927.

[8] a) S. Ahrens, A. Peritz, T. Strassner, *Angew. Chem. Int. Ed.* **2009**, *48*, 7908–7910; *Angew. Chem.* **2009**, *121*, 8048–8051; b) L. Shi, N. Li, L. Zheng, *J. Phys. Chem. C* **2011**, *115*, 18295–18301.

[9] a) H. S. Schrekker, M. P. Stracke, C. M. Schrekker, J. Dupont, *Ind. Eng. Chem. Res.* **2007**, *46*, 7389–7392; b) H. S. Schrekker, D. O. Silva, M. A. Gelesky, M. P. Stacke, C. M. Schrekker, R. S. Gonçalves, J. Dupont, *J. Braz. Chem. Soc.* **2008**, *19*, 426–433; c) Y. Zhao, J. Wang, H. Jiang, Y. Hu, *J. Mol. Liq.* **2014**, *196*, 314–318.

[10] T. Sato, G. Masuda, K. Takagi, *Electrochim. Acta* **2004**, *49*, 3603–3611.

[11] a) W. Xu, C. A. Angell, *Science* **2003**, *302*, 422–425; b) M. Döbbelin, I. Azcune, M. Bedu, A. Ruiz de Luzuriaga, A. Genua, V. Jovanovski, G. Cabañero, I. Odriozola, *Chem. Mater.* **2012**, *24*, 1583–1590; c) L. V. N. R. Ganapatibhotla, J. Zheng, D. Roy, S. Krishnan, *Chem. Mater.* **2010**, *22*, 6347–6360; d) L. C. Branco, J. N. Rosa, J. J. M. Ramos, C. A. M. Alfonso, *Chem. Eur. J.* **2002**, *3*, 3671–3677; e) Z. B. Zhou, H. Matsumoto, K. Tatsumi, *Chem. Eur. J.* **2006**, *12*, 2196–2212.

[12] a) J. E. Bara, C. J. Gabriel, S. Lessmann, T. K. Carlisle, A. Finotello, D. L. Gin, R. D. Noble, *Ind. Eng. Chem. Res.* **2007**, *46*, 5380–5386; b) G. D. Smith, O. Borodin, L. Li, H. Kim, Q. Liu, J. E. Bara, D. L. Gin, R. Nobel, *Phys. Chem. Chem. Phys.* **2008**, *10*, 6301–6312; c) B. Winther-Jensen, K. Fraser, C. Ong, M. Forsyth, D. R. MacFarlane, *Adv. Mater.* **2010**, *22*, 1727–1730.

[13] a) H. S. Schrekker, M. A. Gelesky, M. P. Stracke, C. M. Schrekker, G. Machado, S. R. Teixeira, J. C. Rubim, J. Dupont, *J. Colloid Interface Sci.* **2007**, *316*, 189–195; b) D. Dorjnamjin, M. Ariunaa, Y. K. Shim, *Int. J. Mol. Sci.* **2008**, *9*, 807–820.

[14] a) X. Wang, F. W. Heinemann, M. Yang, B. U. Melcher, M. Fekete, A. V. Mudring, P. Wasserscheid, K. Meyer, *Chem. Commun.* **2009**, 7405–7407; b) X. Wang, C. S. Vogel, F. W. Heinemann, P. Wasserscheid, K. Meyer, *Cryst. Growth Des.* **2011**, *11*, 1974–1988; c) V. Seidl, M. Sternberg, F. W. Heinemann, M. Schmiele, T. Unruh, P. Wasserscheid, K. Meyer, *Cryst. Growth Des.* **2021**, *21*, 6276–6288.

[15] a) T. Schulz, S. Ahrens, D. Meyer, C. Allolio, A. Peritz, T. Strassner, *Chem. Asian J.* **2011**, *6*, 863–867; b) S. Stolte, T. Schulz, C.-W. Cho, J. Arning, T. Strassner, *ACS Sustainable Chem. Eng.* **2013**, *1*, 410–418; c) M. Kaliner, A. Rupp, I. Krossing, T. Strassner, *Chem. Eur. J.* **2016**, *22*, 10044–10049; d) D. H. Zaitsau, M. Kaliner, S. Lerch, T. Strassner, V. N. Emel'yanenko, S. P. Verevkin, *Z. Anorg. Allg. Chem.* **2017**, *643*, 114–119; e) S. Lerch, T. Strassner, *Chem. Eur. J.* **2019**, *25*, 16251–16256; f) F. Schroeter, J. Soellner, T. Strassner, *Chem. Eur. J.* **2019**, *25*, 2527–2537; g) H. Biller, S. Lerch, K. Tolke, H. G. Stammler, B. Hoge, T. Strassner, *Chem. Eur. J.* **2021**, *27*, 13325–13329; h) S. Lerch, T. Strassner, *Chem. Eur. J.* **2021**, *27*, 15554–15557; i) A. A. Fernandez, L. T. de Haan, P. H. J. Kouwer, *J. Mater. Chem. A* **2013**, *1*, 354–357.

[16] P. H. J. Kouwer, T. M. Swager, *J. Am. Chem. Soc.* **2007**, *129*, 14042–14052.

[17] a) K. Goossens, K. Lava, C. W. Bielawski, K. Binnemans, *Chem. Rev.* **2016**, *116*, 4643–4807; b) K. Binnemans, *Chem. Rev.* **2005**, *105*, 4148–4420.

[18] a) F. Glorius, in *N-Heterocyclic Carbenes in Transition Metal Catalysis*, (Ed.: F. Glorius), Springer Verlag, Berlin, Heidelberg, **2007**; b) C. S. J. Cazin, in *N-Heterocyclic Carbenes in Transition Metal Catalysis and Organocatalysis*, (Eds.: C. Bianchini, D. J. Cole-Hamilton, P. W. N. M. van Leeuwen), Springer Verlag, Dordrecht, Heidelberg, London, New York, **2011**; c) H. D. Velazquez, F. Verpoort, *Chem. Soc. Rev.* **2012**, *41*, 7032–7060; d) D. Munz, K. Meyer, *Nat. Chem. Rev.* **2021**, *5*, 422–439; e) D. Munz, C. Allolio, D. Meyer, M. Micksch, L. Roessner, T. Strassner, *J. Organomet. Chem.* **2015**, *794*, 330–335.

[19] S. Ahrens, E. Herdtweck, S. Goutal, T. Strassner, *Eur. J. Inorg. Chem.* **2006**, 1268–1274.

[20] L. Zhu, P. Guo, J. Lan, R. Xie, J. You, *J. Org. Chem.* **2007**, *72*, 8535–8538.

[21] A. Suzuki, *Angew. Chem. Int. Ed.* **2011**, *50*, 6722–6737; *Angew. Chem.* **2011**, *123*, 6854–6869.

[22] a) A. Mishchenko, L. A. Zotti, D. Vonlanthen, M. Bürkle, F. Pauly, J. C. Cuevas, M. Mayor, T. Wandlowski, *J. Am. Chem. Soc.* **2011**, *133*, 184–187; b) E. Leary, A. La Rosa, M. T. Gonzalez, G. Rubio-Bollinger, N. Agrait, N. Martin, *Chem. Soc. Rev.* **2015**, *44*, 920–942.

[23] a) T. Cremer, C. Kolbeck, K. R. Lovelock, N. Paape, R. Wölfel, P. S. Schulz, P. Wasserscheid, H. Weber, J. Thar, B. Kirchner, F. Maier, H.-P. Steinrück, *Chem. Eur. J.* **2010**, *16*, 9018–9033; b) S. Cha, M. Ao, W. Sung, B. Moon, B. Ahlström, P. Johansson, Y. Ouchi, D. Kim, *Phys. Chem. Chem. Phys.* **2014**, *16*, 9591–9601.

[24] a) N. Wang, Z. M. Hudson, S. Wang, *Organometallics* **2010**, *29*, 4007–4011; b) A. K. Mohamed, N. Auner, M. Bolte, *Acta Crystallogr.* **2003**, *E59*, o476-o477; c) F. Lundvall, D. S. Wragg, P. D. Dietzel, H. Fjellvåg, *Acta Crystallogr.* **2014**, *E70*, o449; d) G. Casalone, C. Mariani, A. Mugnoli, M. Simonetta, *Acta Crystallogr.* **1969**, *B24*, 1741–1750.

[25] W. A. Henderson, V. G. Young Jr., D. M. Fox, H. C. De Long, P. C. Trulove, *Chem. Commun.* **2006**, 3708–3710.

[26] a) C. A. Hunter, J. K. M. Sanders, *J. Am. Chem. Soc.* **1990**, *112*, 5525–5534; b) A. L. Ringer, M. O. Sinnokrot, R. P. Lively, C. D. Sherrill, *Chem. Eur. J.* **2006**, *12*, 3821–3828; c) C. Janiak, *J. Chem. Soc. Dalton Trans.* **2000**, 3885–3896.

[27] a) Y. U. Paulechka, G. J. Kabo, A. V. Blokhin, A. S. Shaplov, E. I. Lozinskaya, D. G. Golovanov, K. A. Lyssenko, A. A. Korlyukov, Y. S. Vygodskii, *J. Phys. Chem. B* **2009**, *113*, 9538–9546; b) T. Endo, T. Morita, K. Nishikawa, *Chem. Phys. Lett.* **2011**, *517*, 162–165.

[28] a) Y. Cao, T. Mu, *Ind. Eng. Chem. Res.* **2014**, *53*, 8651–8664; b) S. Sowmiah, V. Srinivasadesikan, M. C. Tseng, Y. H. Chu, *Molecules* **2009**, *14*, 3780–3813.

[29] J. C. Garrison, W. J. Youngs, *Chem. Rev.* **2005**, *105*, 3978–4008.

[30] a) K. M. Lee, H. M. J. Wang, I. J. B. Lin, *J. Chem. Soc. Dalton Trans.* **2002**, 2852–2856; b) C. Hirtenlehner, C. Krims, J. Holbling, M. List, M. Zabel, M. Fleck, R. J. Berger, W. Schoefberger, U. Monkowius, *Dalton Trans.* **2011**, *40*, 9899–9910; c) H. M. J. Wang, I. J. B. Lin, *Organometallics* **1998**, *17*, 972–975; d) S. K. Schneider, W. A. Herrmann, E. Herdtweck, *Z. Anorg. Allg. Chem.* **2003**, *629*, 2363–2370.

[31] a) M. Jansen, *Angew. Chem. Int. Ed. Engl.* **1987**, *26*, 1098–1110; b) K. Singh, J. R. Long, P. Stavropoulos, *J. Am. Chem. Soc.* **1997**, *119*, 2942–2943; c) N. C. Baenzinger, A. W. Struss, *Inorg. Chem.* **1976**, *15*, 1807–1809.

[32] a) A. A. Danopoulos, T. Simler, P. Braunstein, *Chem. Rev.* **2019**, *119*, 3730–3961; b) A. P. Prakasham, P. Ghosh, *Inorg. Chim. Acta* **2015**, *431*, 61–100.

[33] a) D. S. McGuinness, W. Mueller, P. Wasserscheid, K. J. Cavell, B. W. Skelton, A. H. White, U. Englert, *Organometallics* **2002**, *21*, 175–181; b) D. S. McGuinness, K. J. Cavell, *Organometallics* **1999**, *18*, 1596–1605; c) S. Hameury, P. de Frémont, P.-A. R. Breuil, H. Olivier-Bourbigou, P. Braunstein, *Organometallics* **2014**, *34*, 2183–2201; d) J. Berding, M. Lutz, A. L. Spek, E. Bouwman, *Appl. Organomet. Chem.* **2011**, *25*, 76–81; e) E. F. Hahn, B. Heidrich, A. Hepp, T. Pape, *J. Organomet. Chem.* **2007**, *692*, 4630–4638.

[34] a) P. K. Verma, S. Mandal, K. Geetharani, *ACS Catal.* **2018**, *8*, 4049–4054; b) Y. Liu, J. Xiao, L. Wang, Y. Song, L. Deng, *Organometallics* **2015**, *34*, 599–605; c) Y. Liu, L. Wang, L. Deng, *J. Am. Chem. Soc.* **2016**, *138*, 112–115.

[35] a) M. H. Al-Afyouni, V. M. Krishnan, H. D. Arman, Z. J. Tonzetich, *Organometallics* **2015**, *34*, 5088–5094; b) K. Matsubara, T. Sueyasu, M. Esaki, A. Kumamoto, S. Nagao, H. Yamamoto, Y. Koga, S. Kawata, T. Matsumoto, *Eur. J. Inorg. Chem.* **2012**, 3079–3086; c) K. Matsubara, A. Kumamoto, H. Yamamoto, Y. Koga, S. Kawata, *J. Organomet. Chem.* **2013**, *727*, 44–49.

[36] a) J. A. Przyojski, H. D. Arman, Z. J. Tonzetich, *Organometallics* **2013**, *32*, 723–732; b) T. E. Iannuzzi, Y. Gao, T. M. Baker, L. Deng, M. L. Neidig, *Dalton Trans.* **2017**, *46*, 13290–13299; c) K. A. Smart, A. Vanbergen, J. Lednik, C. Y. Tang, H. B. Mansaray, I. Siewert, S. Aldridge, *J. Organomet. Chem.* **2013**, *741–742*, 33–39; d) J. Chai, H. Zhu, Y. Peng, H. W. Roesky, S. Singh, H.-G. Schmidt, M. Noltemeyer, *Eur. J. Inorg. Chem.* **2004**, 2673–2677.

[37] a) K. L. Fillman, J. A. Przyojski, M. H. Al-Afyouni, Z. J. Tonzetich, M. L. Neidig, *Chem. Sci.* **2015**, *6*, 1178–1188; b) J. Louie, R. H. Grubbs, *Chem. Commun.* **2000**, 1479–1480; c) J. J. Dunsford, I. A. Cade, K. L. Fillman, M. L. Neidig, M. J. Ingleson, *Organometallics* **2013**, *33*, 370–377; d) J. A. Przyojski, H. D. Arman, Z. J. Tonzetich, *Organometallics* **2012**, *31*, 3264–3271; e) T. Hashimoto, S. Urban, R. Hoshino, Y. Ohki, K. Tatsumi, F. Glorius, *Organometallics* **2012**, *31*, 4474–4479.

[38] a) E. M. Zolnhofer, M. Käß, M. M. Khusniyarov, F. W. Heinemann, L. Maron, M. van Gastel, E. Bill, K. Meyer, *J. Am. Chem. Soc.* **2014**, *136*, 15072–15078; b) M. Käß, J. Hohenberger, M. Adelhardt, E. M. Zolnhofer, S. Mossin, F. W. Heinemann, J. Sutter, K. Meyer, *Inorg. Chem.* **2014**, *53*, 2460–2470.

[39] T. J. Boyle, R. M. Sewell, L. A. M. Ottley, H. D. Pratt III, C. J. Quintana, S. D. Bunge, *Inorg. Chem.* **2007**, *46*, 1825–1835.

[40] a) A. I. Popov, D. H. Geske, *J. Am. Chem. Soc.* **1958**, *80*, 1340–1352; b) R. T. Iwamoto, *Anal. Chem.* **1959**, *31*, 955; c) I. S. El-Hallag, *J. Chil. Chem. Soc.* **2010**, *55*, 67–73.

[41] G. Bousrez, O. Renier, B. Adranno, V. Smetana, A.-V. Mudring, *ACS Sustainable Chem. Eng.* **2021**, *9*, 8107–8114.